

1 OCT2Hist: Non-Invasive Virtual Biopsy

2 Using Optical Coherence Tomography

3 Yonatan Winetraub^{1,2,3,4,*}, Edwin Yuan^{1,2,5,*}, Itamar Terem^{1,2,6,*}, Caroline Yu^{1,2}, Warren Chan⁷,
4 Hanh Do⁷, Saba Shevidi^{1,2}, Maiya Mao^{1,2}, Jacqueline Yu^{1,2}, Megan Hong^{1,2}, Erick
5 Blankenberg^{1,2}, Kerri E. Rieger⁸, Steven Chu^{3,4,9}, Sumaira Aasi⁷, Kavita Y. Sarin⁷, Adam de la
6 Zerda^{1,2,3,4,6,10,+}

- 7 1. Department of Structural Biology, Stanford University, Stanford, California 94305, USA
- 8 2. Molecular Imaging Program at Stanford, Stanford, California 94305, USA
- 9 3. The Bio-X Program, Stanford, California 94305, USA
- 10 4. Biophysics Program at Stanford, Stanford, California 94305, USA
- 11 5. Department of Applied Physics, Stanford University, Stanford, CA 94305, USA
- 12 6. Department of Electrical Engineering, Stanford University, Stanford, CA 94305, USA
- 13 7. Department of Dermatology, Stanford University School of Medicine, Stanford,
14 California, 94305, USA
- 15 8. Department of Pathology, Stanford University School of Medicine and Stanford Cancer
16 Institute, Stanford, California, 94305, USA
- 17 9. Departments of Physics and Molecular and Cellular Physiology, Stanford University,
18 Stanford, California 94305, USA
- 19 10. The Chan Zuckerberg Biohub, San Francisco, California 94158, USA

20 * These authors contributed equally to this work.

21 + Correspondence Author Email: adlz@stanford.edu

22

23 **Histological haematoxylin and eosin–stained (H&E) tissue sections are used as the gold**
24 **standard for pathologic detection of cancer, tumour margin detection, and disease**
25 **diagnosis¹. Producing H&E sections, however, is invasive and time-consuming. Non-**
26 **invasive optical imaging modalities, such as optical coherence tomography (OCT),**
27 **permit label-free, micron-scale 3D imaging of biological tissue microstructure with**
28 **significant depth (up to 1mm) and large fields-of-view², but are difficult to interpret and**
29 **correlate with clinical ground truth without specialized training³. Here we introduce the**
30 **concept of a virtual biopsy, using generative neural networks to synthesize virtual H&E**
31 **sections from OCT images. To do so we have developed a novel technique, “optical**
32 **barcoding”, which has allowed us to repeatedly extract the 2D OCT slice from a 3D OCT**
33 **volume that corresponds to a given H&E tissue section, with very high alignment**
34 **precision down to 25 microns. Using 1,005 prospectively collected human skin sections**
35 **from Mohs surgery operations of 71 patients, we constructed the largest dataset of H&E**
36 **images and their corresponding precisely aligned OCT images, and trained a conditional**
37 **generative adversarial network⁴ on these image pairs. Our results demonstrate the ability**
38 **to use OCT images to generate high-fidelity virtual H&E sections and entire 3D H&E**
39 **volumes. Applying this trained neural network to *in vivo* OCT images should enable**
40 **physicians to readily incorporate OCT imaging into their clinical practice, reducing the**
41 **number of unnecessary biopsy procedures.**

42 Introduction

43 Histopathology, such as H&E tissue sections, has long been the gold standard for disease
44 diagnosis by clinicians. It provides a view of the tissue down to the micron scale, and is a
45 routine part of diagnostic procedures for both cancer⁵ and non-cancer pathologies⁶, as well as
46 surgical procedures such as intraoperative frozen section analysis and Mohs surgery⁷.

47 However, the current histopathology process is an invasive and time consuming task that can
48 take anywhere from a few hours to several days due to its multiple processing steps, including
49 tissue incision, formalin fixation, paraffin embedding, tissue sectioning and staining¹ (Fig. 1a).

50 A potential alternative to histopathology is biomedical imaging. In particular, optical imaging
51 modalities are among the highest resolution methods for in vivo imaging^{8,9}. In recent years,
52 clinical applications have emerged such as fluorescence-guided surgery¹⁰, autofluorescence
53 imaging for virtual histology staining¹¹, nonlinear microscopy methods for stain-free
54 histopathology¹², stimulated Raman histology for intraoperative brain tumour diagnosis¹³,
55 hyperspectral imaging for cancer margin detection¹⁴ and OCT for skin cancer diagnosis¹⁵. In
56 spite of the high resolution, however, many types of optical image remain challenging for clinical
57 professionals to interpret.

58 This problem is especially evident for coherent modalities, such as OCT, which frequently suffer
59 from poor tissue contrast due to speckle noise¹⁶. Studies of OCT have found high sensitivity and
60 specificity for diagnosing certain dermatological pathologies, such as Basal Cell Carcinoma,
61 based on OCT images¹⁷⁻¹⁹—but only after the clinicians received extensive training in
62 interpreting images. Despite OCT's demonstrated suitability for use with epithelial cancers such
63 as skin cancer, it has found only a limited clinical role as a diagnostic tool for these cancers in
64 practice^{20,21}.

65 In this work, we introduce a novel 3D virtual biopsy technology (“OCT2Hist”), designed to
66 circumvent the complications of traditional biopsy by using a generative neural network⁴ to
67 transform OCT images into H&E histology-like images (Fig. 1). This approach offers many
68 significant advantages: OCT is quick and entirely non-invasive, acquiring a single 2D image
69 within milliseconds¹⁵. It requires neither the lengthy tissue preparation procedures nor the
70 significant material and personnel resources needed for traditional biopsy. Furthermore, by non-

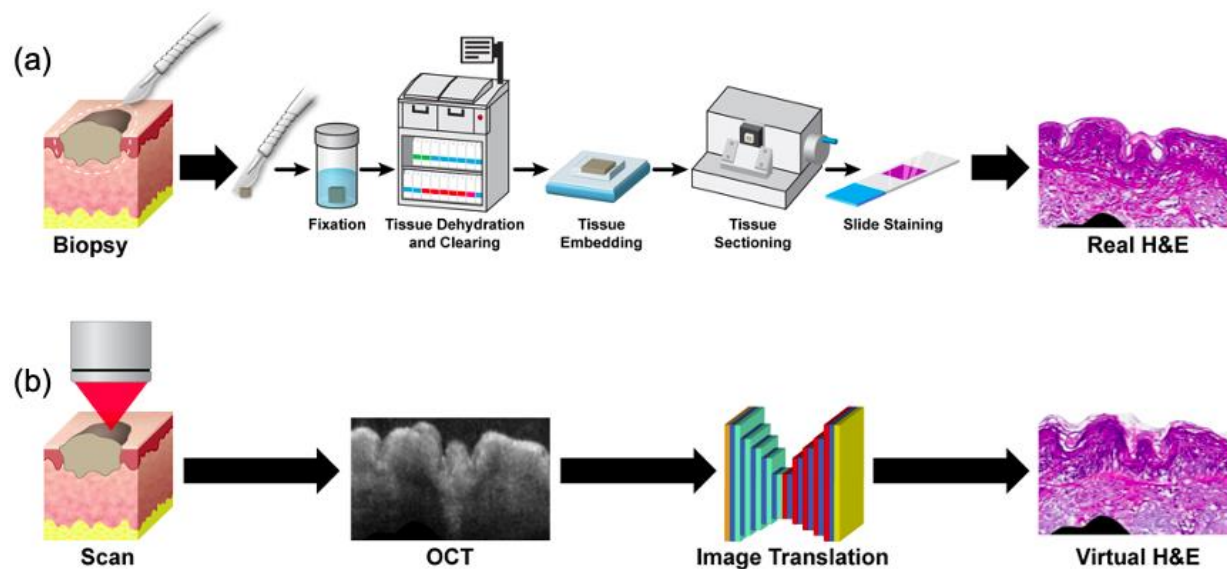
71 invasively acquiring multiple images over time, the technique would be far more suitable for
72 tracking the development of a disease *in vivo*.

73 However, image-to-image translation with neural networks has stringent data requirements for a
74 task to be learned successfully. Ideally, the training examples should be well-aligned to facilitate
75 learning. In our case, each OCT image must be registered to its corresponding H&E image with
76 the highest precision possible⁴. High resolution registration of medical images with H&E images
77 requires a precise match in 9 degrees of freedom (3 translations, 3-axis rotations, and
78 shrinkage/scale change in all axis) and had not previously been adequately achieved²², and
79 certainly not in a systematic and repeatable manner²². Previous work relied on tissue
80 landmarks, careful orientation of tissue cutting, and substantial luck to arrive at an acceptable
81 OCT-H&E image pair.²³ Even in the best-case scenario, it was difficult to correlate tissue
82 features in the OCT with those in the H&E image with high precision. We estimate the
83 registration precision achieved using these methods was 500 microns at best.

84 Results

85 To overcome this registration issue, we developed a novel method of “optical barcoding” that
86 allows us to compute the 2D plane within a 3D OCT volume that corresponds to a particular 2D
87 histology image (Fig. 2). With this technique we assembled a database of 1,005 aligned OCT–
88 H&E image pairs of human skin samples. The precision of alignment was better than 25
89 microns, about an order of magnitude better than the state of the art. These image pairs were
90 aligned with sufficient precision to train a conditional generative adversarial network (cGAN) to
91 perform image-to-image translation from OCT images to H&E-like images. Tests of this
92 translation process on OCT images of new skin samples showed a very high level of agreement
93 between our generated H&E-like images and the corresponding actual H&E sections of the new

94 samples. Our OCT2Hist system has thereby demonstrated a proof-of-principle of the virtual
95 biopsy concept.



96
97 **Figure 1:** Traditional biopsy versus virtual biopsy. (a) In a traditional biopsy, tissue is first
98 excised, and then undergoes multiple steps including fixation, dehydration, clearing, embedding,
99 sectioning and staining to yield 2D H&E sections which can be examined under a microscope.
100 (b) For a virtual biopsy, an OCT scan of tissue is acquired, and a trained neural network:
101 OCT2Hist transforms the 2D OCT image into a corresponding H&E-like image.

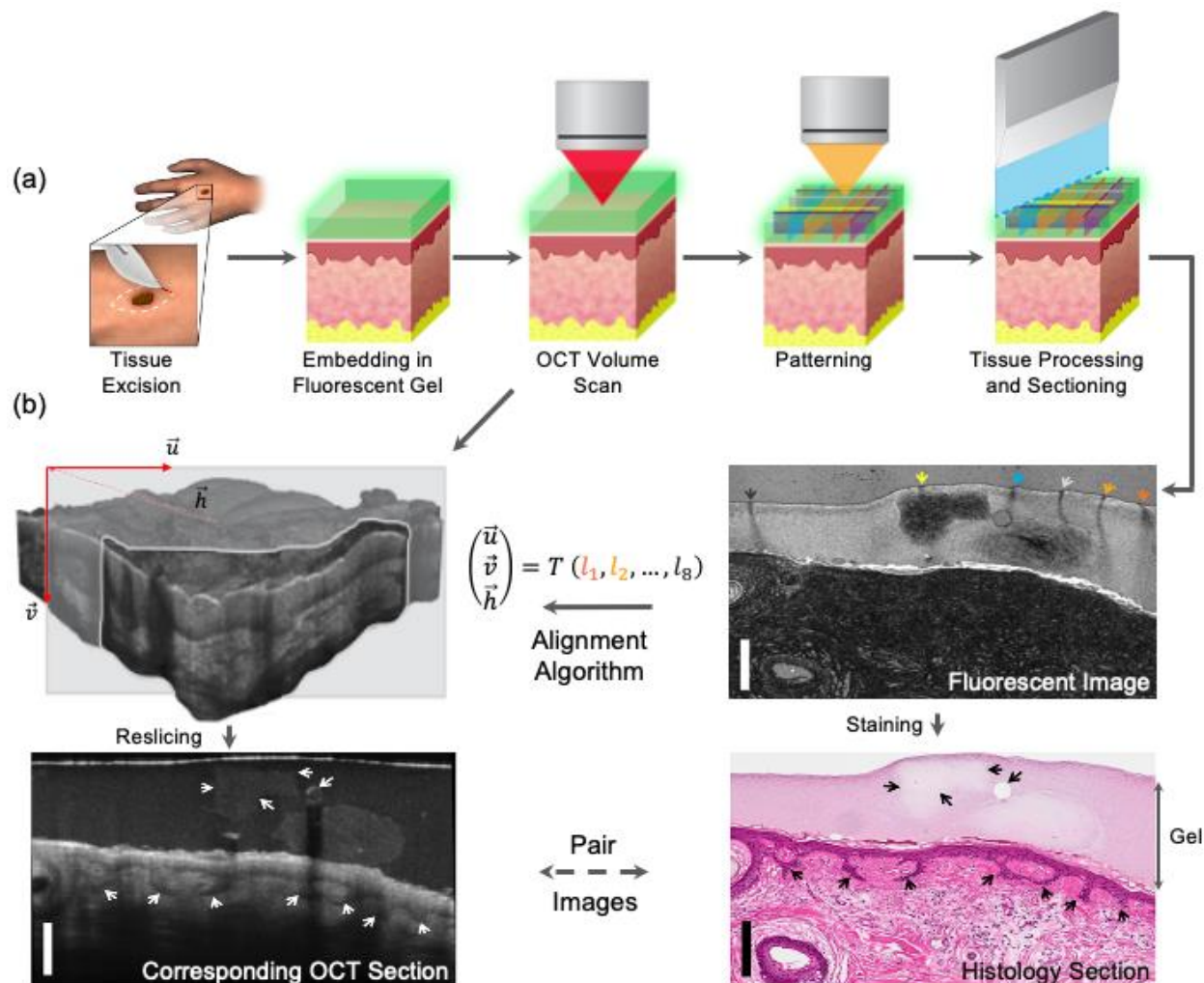
102 Alignment using optical barcoding

103 Our optical barcoding method relies on encasing a freshly excised tissue sample within a
104 transparent fluorescent agar-gelatin gel (Fig. 2; see also Methods section below and
105 Supplementary Materials). We acquire a 3D OCT volume image of the tissue within the gel, and
106 then a specific geometric pattern is photobleached into the gel by a second laser wavelength
107 sent through the OCT optical system (Fig 2a). This pattern forms a barcode marker that is
108 preserved through the standard histological process and encodes all orientation, position and

109 scaling information about how the section was cut (Fig 2b). An alignment algorithm uses the
110 appearance of this marker in the histology image to compute a 2D reslice of the OCT volume
111 that corresponds in one-to-one fashion with the histology image. Our technique is repeatable
112 and we regularly achieve registration precision down to 25 microns, as verified by bead-in-gel
113 experiments (Fig. S7) and by correlating features between the OCT and histology images (Fig.
114 S8).

115
116 We applied this barcoding technique to histology sections from 119 human skin samples freshly
117 excised during Mohs surgery (IRB-24307), thereby assembling a large dataset of aligned OCT–
118 H&E image pairs. In addition to the alignment computed from the optical barcode, we manually
119 performed additional fine alignment of the OCT-H&E image pairs based on tissue features
120 within both images, to achieve the highest quality of alignment possible. We removed samples
121 with low-quality alignment, or low quality of either OCT or H&E images, and arrived at a dataset
122 of 1,005 aligned OCT-H&E image pairs (one image pair per histology section) taken from 71 of
123 the skin samples. The dataset was subject to further digital processing for stain color
124 normalization and removal of low-SNR image regions, before the images were used for the
125 machine learning task.

126



127

128

129 **Figure 2:** Illustration of the optical barcoding method used to create precisely aligned OCT-H&E

130 image pairs from ex vivo tissue samples. (a) Top row, left to right: The collected tissue

131 specimen is encased in the fluorescent gel, after an OCT volume scan is taken and a diode

132 laser patterns the optical barcode by photobleaching the fluorescent gel, then the tissue

133 undergoes histological processing and tissue sectioning. (b) The tissue section is imaged (top

134 right) to produce a 2D fluorescence image containing the optical barcode (denoted by the

135 colored arrows), and then H&E stain (bottom right). The barcode is used to reslice the 3D OCT

136 volume (top left) and to extract a 2D OCT image (bottom left) that physically corresponds to the

137 H&E section (bottom right). The black and white arrows pointing to strands of epithelial cells in

138 the epithelium as well as a gelatin chunk in the tissue-encasing gel in both H&E and its
139 corresponding OCT images).

140

141 Machine learning

142 To produce our OCT2Hist image translator, we developed a conditional GAN model based on
143 the pix2pix framework, but with some changes which were found to improve the quality of the
144 generated images. We trained our cGAN model⁴ on the dataset of 553 high-quality OCT-H&E
145 image pairs from 38 patients (54% of dataset). We then tested its performance on patient
146 samples that it had not encountered before (452 high-quality OCT-H&E image pairs from the
147 other 33 patients). Our training data included a large number of skin samples from the scalp and
148 regions of the face and neck, and smaller numbers from the legs and chest (Fig. 3a, S14, S15).

149 Figure 3b–d shows example test results of OCT images from the face and forearm, each one
150 alongside the virtual H&E generated by the neural network, and the real H&E that the OCT slice
151 had been aligned to by our barcoding method. In the OCT images, the nuclei-rich epithelial layer
152 appears darker, while the highly scattering connective tissue of the stroma tends to appear
153 brighter. The generated H&E images demonstrate the neural network’s understanding of these
154 features.

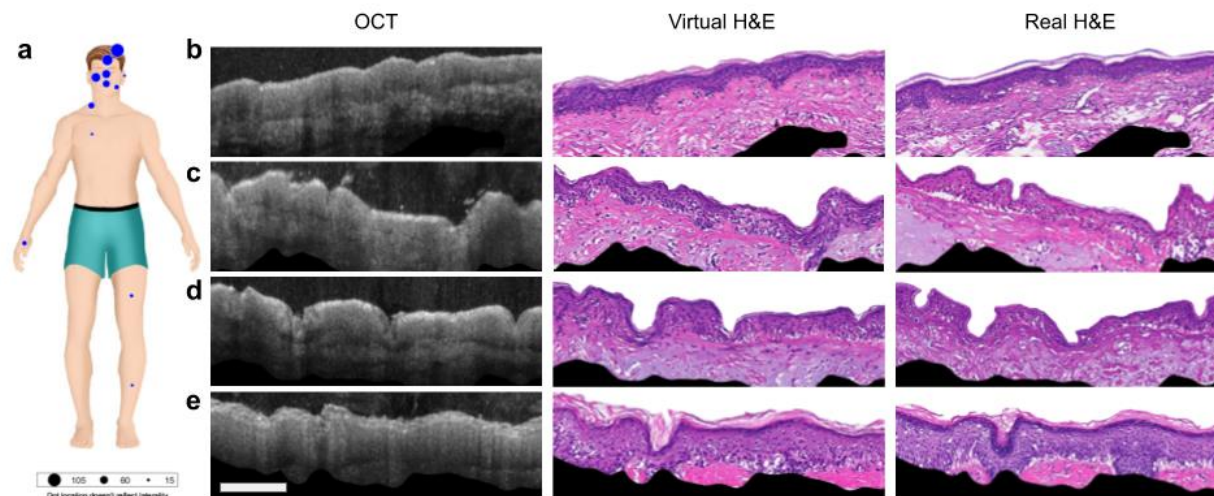
155

156 The first sample from the face (Fig. 3b) has a well-defined epithelial layer and strong signal and
157 contrast within the stroma. Notice that the epithelium shrinks during histological processing, and
158 the image translator takes this into account, accurately reproducing the epithelial thickness of
159 the H&E images. Part of a hair follicle is also visible on the left side of the H&E image. The
160 follicle is less apparent in the virtual H&E image, possibly due to imperfect alignment or difficulty
161 seeing it in the OCT image. The final sample (Fig. 3d) is of arm skin with ridge-like epithelium.

162 Interestingly, the neural network generated a high quality H&E virtual image despite seeing no
163 examples of arm skin in its training set. It is also recognized from the OCT image that this
164 sample has characteristics of sun damage, as seen in discolored, lighter gray tissue found
165 throughout the stroma of both the virtual and ground truth H&E. Most test set samples show
166 similar results (Fig. S17).

167
168 To further test the quality of the virtual H&E images, we randomly selected 70 H&E images (35
169 real, 35 virtual) from different patients in the test set, and gave them to two pathologists to
170 assess in a double-blind experiment. The pathologists correctly determined whether a biopsy
171 image was real or virtual only 69% of the time, indicating that the virtual images are not easily
172 distinguishable from real ones. We believe that by further increasing the training set, we can
173 further improve neural network performances (see Supplementary Materials).

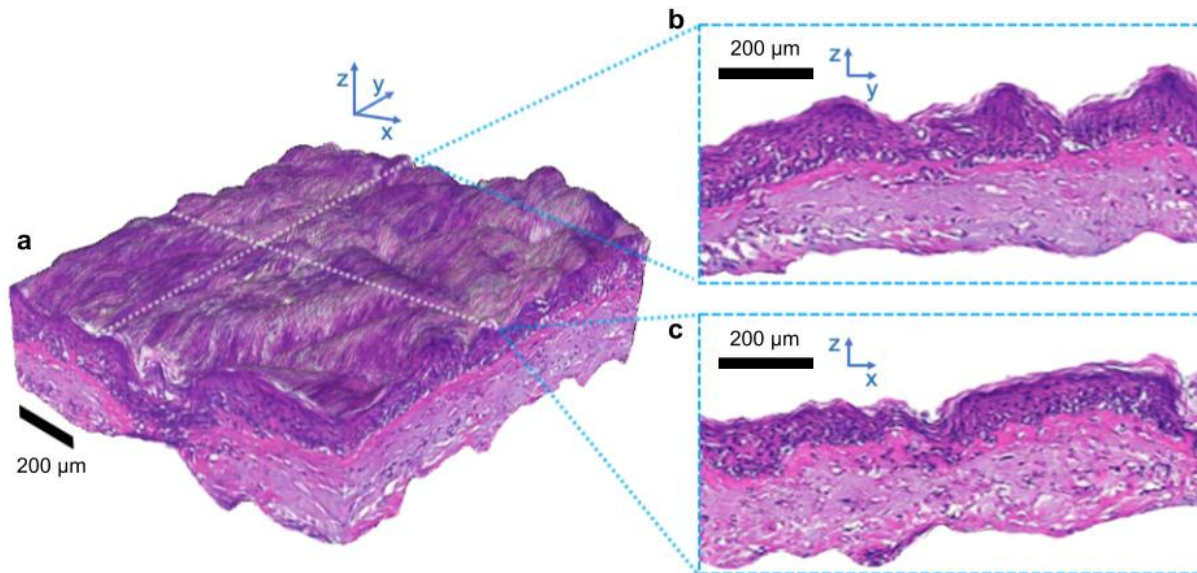
174 By generating virtual H&E images slice-by-slice, we can also create an entire virtual H&E
175 volume from a corresponding OCT volume (Fig. 4). The virtual H&E volume can be resliced
176 from either axis (Fig. 4B,C, Supplementary Video). The ability to create such a representation
177 provides a powerful, efficient and intuitive way of collecting H&E-like data from a patient and
178 presenting it to a clinician, avoiding the randomness and imprecision of the sectioning
179 process^{24,25}, where only a few slices from an entire tissue block can be examined under a
180 microscope.



181

182

183 **Figure 3:** Generating virtual histology H&E images from OCT. (a) Locations of biopsies used in
184 our training set (blue dots). Panel at right shows examples (from the testing set) of an OCT
185 image, the computer generated virtual H&E image, and the corresponding actual histology
186 image from face region where we had a dense training set (b,c,d), and from the forearm (e)
187 where we had no nearby training set. Features as small as tens of microns in size, as found in
188 the shape of the epithelium, are matched. We do not expect smaller features to match as our
189 OCT scanner does not have the resolution or information density to accurately generate smaller
190 features. Scale bar is 200 microns.



191
192 **Figure 4:** A 3D virtual H&E volume generated slice-by-slice from an OCT volume. The volume
193 can be viewed in multiple ways, including isometric projection (a) and 2D cross-sectional views
194 from within the volume (b, c), which can be chosen to slice across any plane.

195 Discussion

196 Our work has demonstrated a proof-of-concept of the 3D virtual biopsy approach: the
197 generation of highly realistic virtual H&E sections directly from OCT images. This result in turn
198 relied on the feasibility of using our optical barcoding technique to create a large database of
199 accurately aligned pairs of OCT and H&E histology images. These aligned image pairs were
200 essential for generating high quality virtual histology images with our cGAN, and tests using an
201 alternative cGAN that is trainable without aligned images generated output images of much
202 lower quality (Fig. S12).

203

204 There are two primary directions for taking this work further, which we anticipate will open the
205 door for a variety of basic research and clinical applications. First, optical barcoding can be used

206 to obtain the precise H&E ground truth of OCT images as well as other types of optical image.
207 Obtaining reliable ground truth enables multiple applications such as verifying the binding of
208 contrast agents, better understanding how different structures may be distorted in histology, or
209 for obtaining data needed to train other machine learning algorithms, such as ones designed to
210 directly classify cancers or other abnormalities from an OCT image.

211
212 Second, our OCT2Hist process can be applied and further developed for a variety of basic and
213 clinical research applications. Once it is properly trained, the image translator can be used to
214 produce virtual H&E images without any need to optically barcode the OCT-imaged tissue. Thus
215 it can be used non-invasively in vivo either to diagnose various superficial skin cancers or to
216 confirm tumour margins, bypassing the invasive, time-consuming, and costly biopsy and
217 histological processing procedure¹. This is particularly important in cases where small tumours
218 may have been completely eradicated by the biopsy and subsequent cascade of inflammation:
219 There is no non-invasive modality available to determine whether surgery is still indicated
220 without making an incision that can lead to scarring on the patient's skin, which is particularly
221 undesirable on the face²⁶.

222
223 We note several shortcomings of the present machine learning algorithm. The first is that
224 because we had to run on freshly excised tissues, we used a relatively small dataset to train our
225 model of 1,005 images from 71 patients. Modern cGANs are trained on an order of magnitude
226 more data, which makes the model more robust and generalizable to not-previously-seen
227 samples. We expect our model to generate even more robust epithelial structures, textures and
228 stromal features as the training dataset increases. As is well documented for deep learning
229 applications, we expect the quality and robustness of OCT2Hist's results to scale with the
230 amount of data collected^{27,28}.

231

232 A second limitation is the relatively small amount of information present in OCT images due to
233 resolution, signal quality and contrast mechanism. OCT image resolution sets a lower limit on
234 the size of features that can be reliably generated by the neural network. In practice, speckle
235 noise^{1629,30} and multiple scattering³¹ can further obfuscate the useful information within a voxel.
236 For this reason, in this paper we focused on generating large features (>50 microns) that have
237 sufficient reliable information in the OCT image. Although our algorithm generates fine histology
238 features such as cell nuclei, we believe that they should be regarded as general texture features
239 and not interpreted as the exact position of individual cells as current OCT signal quality does
240 not allow us to capture this information. In our training and testing, we specifically addressed the
241 issue of lack of OCT signal in certain regions of the image (due to optical extinction) by masking
242 out low-signal regions in both OCT and H&E images. The optical extinction also limits the
243 imaging depth, which we typically observed was up to 450 microns for reasonable signal-to-
244 noise ratio for the machine learning algorithm. We believe that future work based on OCT
245 systems with higher spatial resolution, such as commercial systems with the capability to
246 reliably image single cells³²⁻³⁴, will yield virtual H&E images of significantly higher quality. Most
247 importantly, the principles developed in this work are easily translatable to such higher
248 resolution OCT systems.

249
250 We believe that our OCT2Hist model can pave the way for a true virtual biopsy that is able to
251 generate intuitive H&E-like images, supporting clinical decision-making in dermatology by
252 identifying tumour margins and confirming tumour diagnosis. We further believe our optical
253 barcoding method can shed light on the relationship between structures seen in OCT, confocal
254 microscopy and other optical methods and a histopathological section of the exact same area.

255
256 An immediate next step will be to demonstrate that the model can robustly generate H&E-like
257 features of superficial basal-cell carcinoma (BCC), including cancer margins, from OCT images.

258 This is a favourable test case, as BCC clusters are typically hundreds of microns in size^{21,35},
259 putting them well within the range of our system. As a preliminary result, we added a few cancer
260 samples to our training set and show feasibility for non-invasive BCC detection (Fig. S18).

261 Methods

262 Our image-alignment and cGAN-training pipeline featured several steps: encasing the tissue in
263 fluorescent gel, OCT imaging, writing the optical barcode by photobleaching, computationally
264 extracting the reslice parameters from the optical barcode, user-performed fine alignment of the
265 OCT-H&E image pairs, quality assurance, stain color normalization, removal of low SNR
266 regions from image, and finally machine learning training. Additional information is in the
267 Supplementary Materials.

268 Sample extraction

269 All participants provided verbal consent to participate in this study under IRB-24307. We
270 received fresh tissue samples daily from Mohs surgery operations. Samples were stored and
271 transferred in keratinocyte media consisting of DMEM/F12 containing penicillin/streptomycin
272 (0.1%); fungizone (40 µg/ml); B27 (without vitamin A), epidermal growth factor (20 ng/ml), and
273 basic fibroblast growth factor (40 ng/ml; Sigma) to support cell viability and were processed
274 within 4 hours after excision. Prior to processing, tissues samples were transected to create a
275 smaller size of approximately 0.5 cm x 0.25 cm x 0.5 cm.

276 Gel encasement

277 Each tissue block was encased in a fluorescent gel. The gel was produced by mixing 0.03 g of
278 Knox gelatin with water and 50 µL of 50 µM Alexa 680-NHS Ester dye in a glass flask, and

279 mixing on a tilt table for 10 min. We added 0.06 g of agar and an additional 0.045 g of gelatin to
280 the mixture before bringing the mixture to a boil in the microwave (about 10 s). The mixture was
281 cooled for 10 s and then poured over the tissue sample resting in a cassette. After about 5 min
282 at room temperature, the liquid mixture completely solidified to a gel.

283 OCT imaging and barcoding

284 Each encased sample was placed on an XYZ translation stage (Thorlabs MT3-Z8) for imaging
285 and barcoding. All images were collected with a Thorlabs Ganymede OCT system (Thorlabs
286 GAN220). The optical fiber transmitting light to the scanhead was replaced with a custom-made
287 wavelength division multiplexer with two input ports (for the photobleaching laser and the OCT
288 source) and one output port. The OCT system was outfitted with a 10x, long-working-distance
289 objective lens (Olympus UMPLFLN10XW) with an effective numerical aperture of 0.2, which
290 was used with silicone oil immersion ($n=1.4$, which approximately matches the refractive index
291 of skin tissue).

292
293 We collected 48 volume scans of 1 x 1 mm, where the optical focus was translated by 10 μm
294 between each scan by a z-axis translation of the sample. All volumes were then computationally
295 stitched together to yield an OCT volume with isotropic lateral resolution. After imaging was
296 completed, a 650 nm laser diode (LP660-SF50) was activated (about 3.3 mW at output) to
297 photobleach the optical barcode with 2 passes per line, at a line rate of 1 mm/15 s. Afterwards,
298 an overview scan (Supplementary Figure S4) of total size 7x8 mm, consisting of 1x1 mm tiles
299 scans was taken. The overview scan was used to determine a specific distance to cut into the
300 tissue block in order to reach the location of the optical barcode.

301 H&E preparation

302 The gel-encased, bar-coded tissue was then submerged in formalin solution for 24 h, and then
303 transferred to 30% ethanol solution for about 2 h. The sample then underwent histological
304 processing (protocol is shown in Figure S5), and the two-iteration cutting procedure (described
305 in the subsection “Histological Processing & Tissue Sectioning” of the Supplementary Materials)
306 designed to capture tissue sections in the most optimal location relative to the optical barcode.
307 From each tissue sample we ultimately received 15 unstained tissue sections, which were
308 imaged in a Leica SP5 microscope with a 633 nm emission filter to capture the fluorescent
309 optical barcode on each section. The sections were then H&E stained and white-light images
310 scanned at 20x magnification in an Aperio Digital Pathology Slide Scanner.

311 Alignment

312 The H&E sections were aligned to resliced OCT images using in-house code that allows the
313 user to select the photobleached lines from each fluorescent slide image. The alignment
314 parameters computed directly from the algorithm constitute the “stack alignment”. We then
315 performed a manual “fine alignment” step, where the resliced OCT image was fine-tuned to
316 match the H&E image by adjusting the translation in 3 axes and in-plane rotation.

317
318 Images were filtered based on H&E image quality, OCT image quality, and alignment quality.
319 We cropped OCT-H&E image pairs to 1024x512 pixels at 10x magnification (1 $\mu\text{m}/\text{pixel}$). We
320 masked out areas of the image where the OCT signal did not have a sufficient signal to noise
321 ratio to prevent the neural network from hallucinating tissue features where there is low signal in
322 the OCT image. The results in this work were obtained by training the pix2pix model on the
323 OCT-H&E image crops, which are automatically resized to 256x256 at runtime within the pix2pix

324 preprocessing code. The model also outputs test results at 256x256, which are resized within
325 an external code base to 1024x512.

326

327 The pix2pix model was modified to use the resnet9 generator, with 50% dropout, and with
328 additional training-time data augmentation of random image translation. Use of the resnet9
329 generator (11.4 million parameters), compared to the baseline U-net network (54.4 million
330 parameters), was found to improve generator mode collapse issues. The random translations,
331 which consisted of random translations of up to 50% of the image's length on each axis, were
332 found to improve the quality of generated image features, such as hair follicles and epithelial
333 structures.

334 Acknowledgements

335 This work was funded in part by grants from the United States Air Force (FA9550-15-1-0007), the
336 National Institutes of Health (NIH DP50D012179, K23CA211793), the National Science
337 Foundation (NSF 1438340), the Damon Runyon Cancer Research Foundation (DFS# 06-13),
338 Claire Giannini Fund, the Susan G. Komen Breast Cancer Foundation (SAB15-00003), the Mary
339 Kay Foundation (017-14), the Skippy Frank Foundation, the Donald E. and Delia B. Baxter
340 Foundation, a seed grant from the Center for Cancer Nanotechnology Excellence and Translation
341 (CCNE-T; NIH-NCI U54CA151459), and the Stanford Bio-X Interdisciplinary Initiative Seed Grant
342 (IIP6-43). Y.W. is grateful for a Stanford Bowes Bio-X Graduate Fellowship, Stanford Biophysics
343 Program training grant (T32GM-08294). I.T. is grateful for NSF graduate fellowship. A.D.Z. is a
344 Chan Zuckerberg Biohub investigator and a Pew-Stewart Scholar for Cancer Research supported
345 by The Pew Charitable Trusts and The Alexander and Margaret Stewart Trust. K.Y.S. is the D.
346 G. "Mitch" Mitchell Clinical Investigator supported by the Damon Runyon Cancer Research
347 Foundation (CI-104-19).

348

349 Additionally we would like to thank Anh Ngoc Diep, Murray Resnick, Bhargavi Garimella, Bryan

350 Ronain Smith, Elliot SoRelle, Kent Lee, Lily Nguyen, Madeline Rose Hays, Max Prigozhin, Peng

351 Si, Tommy Winetraub, Vivian Hua, Pauline Chu, Ziv Lautman, Jim Strommer and Graham P

352 Collins.

353 References

- 354 1. Strayer, D. S., Saffitz, J. E. & Rubin, E. *Rubin's Pathology: Mechanisms of Human Disease*.
355 (Lippincott Williams & Wilkins, 2019).
- 356 2. Drexler, W. & Fujimoto, J. G. *Optical Coherence Tomography: Technology and*
357 *Applications*. (Springer Science & Business Media, 2008).
- 358 3. Website. Yow A.P. et al. (2020) Techniques and Applications in Skin OCT Analysis. In: Lee
359 G., Fujita H. (eds) Deep Learning in Medical Image Analysis. Advances in Experimental
360 Medicine and Biology, vol 1213. Springer, Cham. [https://doi.org/10.1007/978-3-030-33128-](https://doi.org/10.1007/978-3-030-33128-3_10)
361 [3_10](https://doi.org/10.1007/978-3-030-33128-3_10).
- 362 4. Isola, P., Zhu, J.-Y., Zhou, T. & Efros, A. A. Image-to-Image Translation with Conditional
363 Adversarial Networks. *2017 IEEE Conference on Computer Vision and Pattern Recognition*
364 *(CVPR)* (2017) doi:10.1109/cvpr.2017.632.
- 365 5. Eberle, F. C., Mani, H. & Jaffe, E. S. Histopathology of Hodgkin's Lymphoma. *Cancer J.*
366 *Sci. Am.* **15**, 129 (2009).
- 367 6. Gupta, E., Bhalla, P., Khurana, N. & Singh, T. Histopathology for the diagnosis of infectious
368 diseases. *Indian J. Med. Microbiol.* **27**, 100–106 (2009).
- 369 7. Mariwalla, K., Aasi, S. Z., Glusac, E. J. & Leffell, D. J. Mohs micrographic surgery
370 histopathology concordance. *J. Am. Acad. Dermatol.* **60**, 94–98 (2009).
- 371 8. Fujimoto, J. G. Optical coherence tomography for ultrahigh resolution in vivo imaging.
372 *Nature Biotechnology* vol. 21 1361–1367 (2003).
- 373 9. Yang, W. & Yuste, R. In vivo imaging of neural activity. *Nature Methods* vol. 14 349–359
374 (2017).
- 375 10. Nguyen, Q. T. & Tsien, R. Y. Fluorescence-guided surgery with live molecular navigation —
376 a new cutting edge. *Nature Reviews Cancer* vol. 13 653–662 (2013).

- 377 11. Rivenson, Y. *et al.* Virtual histological staining of unlabelled tissue-autofluorescence images
378 via deep learning. *Nat Biomed Eng* **3**, 466–477 (2019).
- 379 12. Tao, Y. K. *et al.* Assessment of breast pathologies using nonlinear microscopy.
380 *Proceedings of the National Academy of Sciences* vol. 111 15304–15309 (2014).
- 381 13. Hollon, T. C. *et al.* Near real-time intraoperative brain tumor diagnosis using stimulated
382 Raman histology and deep neural networks. *Nat. Med.* **26**, 52–58 (2020).
- 383 14. Fei, B. *et al.* Label-free reflectance hyperspectral imaging for tumor margin assessment: a
384 pilot study on surgical specimens of cancer patients. *J. Biomed. Opt.* **22**, 1–7 (2017).
- 385 15. Olsen, J., Holmes, J. & Jemec, G. B. E. Advances in optical coherence tomography in
386 dermatology—a review. *Journal of Biomedical Optics* vol. 23 1 (2018).
- 387 16. Schmitt, J. M., Xiang, S. H. & Yung, K. M. Speckle in Optical Coherence Tomography.
388 *Journal of Biomedical Optics* vol. 4 95 (1999).
- 389 17. Fisher, J. *et al.* Clinical Utility of Bedside Multibeam Optical Coherence Tomography
390 Imaging in a Patient With Multiple Basal Cell Carcinomas. *Dermatologic Surgery* vol. 44
391 874–876 (2018).
- 392 18. Ulrich, M. *et al.* The sensitivity and specificity of optical coherence tomography for the
393 assisted diagnosis of nonpigmented basal cell carcinoma: an observational study. *Br. J.*
394 *Dermatol.* **173**, 428–435 (2015).
- 395 19. Li, G. High-Definition Optical Coherence Tomography in the Diagnosis of Basal Cell
396 Carcinoma Evaluated by an Experienced Versus Inexperienced Investigator. *Journal of*
397 *Clinical & Experimental Dermatology Research* vol. 5 (2014).
- 398 20. Cunha, D. *et al.* Comparison of ex vivo optical coherence tomography with conventional
399 frozen-section histology for visualizing basal cell carcinoma during Mohs micrographic
400 surgery. *Br. J. Dermatol.* **165**, 576–580 (2011).
- 401 21. Boone, M. A. L. M., Norrenberg, S., Jemec, G. B. E. & Del Marmol, V. Imaging of basal cell
402 carcinoma by high-definition optical coherence tomography: histomorphological correlation.

- 403 A pilot study. *Br. J. Dermatol.* **167**, 856–864 (2012).
- 404 22. Chicherova, N., Fundana, K., Müller, B. & Cattin, P. C. Histology to microCT data matching
405 using landmarks and a density biased RANSAC. *Med. Image Comput. Comput. Assist.*
406 *Interv.* **17**, 243–250 (2014).
- 407 23. Yecies, D. *et al.* Speckle modulation enables high-resolution wide-field human brain tumor
408 margin detection and in vivo murine neuroimaging. *Sci. Rep.* **9**, 10388 (2019).
- 409 24. Mehra, K. K. *et al.* The impact of tissue block sampling on the detection of p53 signatures in
410 fallopian tubes from women with BRCA 1 or 2 mutations (BRCA+) and controls. *Mod.*
411 *Pathol.* **24**, 152–156 (2011).
- 412 25. Dyson, S. W. *et al.* Impact of thorough block sampling in the histologic evaluation of
413 melanomas. *Arch. Dermatol.* **141**, 734–736 (2005).
- 414 26. Bailin, P. L. & Bailin, M. D. Correction of depressed scars following Mohs' surgery: the role
415 of collagen implantation. *J. Dermatol. Surg. Oncol.* **8**, 845–849 (1982).
- 416 27. Cho, J., Lee, K., Shin, E., Choy, G. & Do, S. How much data is needed to train a medical
417 image deep learning system to achieve necessary high accuracy? *arXiv [cs.LG]* (2015).
- 418 28. Chartrand, G. *et al.* Deep Learning: A Primer for Radiologists. *Radiographics* **37**, 2113–
419 2131 (2017).
- 420 29. Winetraub, Y., Wu, C., Collins, G. P., Chu, S. & de la Zerda, A. Upper limit for angular
421 compounding speckle reduction. *Appl. Phys. Lett.* **114**, 211101 (2019).
- 422 30. Winetraub, Y., SoRelle, E. D., Liba, O. & de la Zerda, A. Quantitative contrast-enhanced
423 optical coherence tomography. *Appl. Phys. Lett.* **108**, 023702 (2016).
- 424 31. Yu Kirillin, M., Priezhev, A. V. & Myllylä, R. Role of multiple scattering in formation of OCT
425 skin images. *Quantum Electron.* **38**, 570 (2008).
- 426 32. Dubois, A. *et al.* Line-field confocal optical coherence tomography for high-resolution
427 noninvasive imaging of skin tumors. *J. Biomed. Opt.* **23**, 1–9 (2018).
- 428 33. Breugnot, J. *et al.* Comparison between LC-OCT imaging and histology to quantify the

- 429 superficial dermis thickness. in JW3A.21 (Optical Society of America, 2020).
- 430 34. Yin, B., Hyun, C., Gardecki, J. A. & Tearney, G. J. Extended depth of focus for coherence-
431 based cellular imaging. *Optica* **4**, 959–965 (2017).
- 432 35. Mandache, D. *et al.* Basal cell carcinoma detection in full field OCT images using
433 convolutional neural networks. *2018 IEEE 15th International Symposium on Biomedical
434 Imaging (ISBI 2018)* (2018) doi:10.1109/isbi.2018.8363689.

435 Author Information

436 Author Contributions:

437 Y.W. conceived of the presented idea. Y.W. developed the theory behind the alignment
438 algorithm. Y.W., E.Y. and I.T. performed the computation of the alignment algorithm. E.Y. and
439 Y.W. performed numerical simulations for the alignment. E.Y., I.T. and Y.W. developed the
440 machine learning theory and performed the computation. Software supporting this project was
441 developed by Y.W., E.Y., I.T. and E.B.. I.T., E.Y., Y.W., C.Y. and E.B. developed and
442 performed instruments calibration. Y.W., E.Y., I.T. C.Y., S.S. and M.H. developed the gel
443 embedding protocol used in the alignment step. S.A., W.C, H.D. collected samples from patients
444 and coordinated secure transportation to our imaging facility. C.Y., S.S., M.M, J.Y., M.H. imaged
445 and processed samples to generate the dataset used in this paper.

446

447 A.D.Z., K.Y., S.A., S.C. and K.E.R. contributed to the overall design and direction of the
448 research.

449

450 The manuscript was written through contributions of all authors. All authors have given approval
451 to the final version of the manuscript.

452

453 Conflict of interest: The authors declare no competing financial interest.

454 Corresponding Author: Correspondence and requests for materials should be addressed to

455 Adam de la Zerda, E-mail: adlz@stanford.edu

456 Supporting Information

457 Supplementary Information is available for this paper.

458 Additional description of the materials, methods, and results; Figures S1–S18 (PDF).

459 Movie S1 showing a 3D rendering of one of virtual histology volumes (MP4).

460 Data

461 The data that support the findings of this study are available from the corresponding author upon

462 reasonable request.